ACS APPLIED ELECTRONIC MATERIALS

pubs.acs.org/acsaelm Article

Large-Area, Flexible, and Dual-Source Co-Evaporated $Cs_3Cu_2I_5$ Nanolayer to Construct Ultra-Broadband Photothermoelectric Detector from Visible to Terahertz

Yunzhi Gu,[#] Xiang Yao,*[,#] Huaxiu Geng, Mengying Long, Guijian Guan, Minglie Hu,* and Mingyong Han

Cite This: *ACS Appl. Electron. Mater.* 2022, 4, 663−671 Read Online

ACCESS | Metrics & More | Article Recommendations | Supporting Information

ABSTRACT: Metal halides show a powerful potential to fabricate photothermoelectric (PTE) detectors due to their merits of ultra-low thermal conductivity, high Seebeck coefficient, and high carrier mobility. It is critically important to develop a flexible, transparent, and large-area PTE material for pushing its practical and extensive application. In this report, we fabricate a PTE-based detector employing lead-free $Cs_3Cu_2I_5$ nanolayered film, which is prepared on a large area using a dual-source co-evaporation technique. Importantly, the PTE detector exhibits self-powered light response wavelengths ranging from visible (532 nm) to near-infrared (980 nm) to terahertz (119 μm). Moreover, we find that the photocurrent generation of the $Cs_3Cu_2I_5$ photodetector by employing lateral device architecture is mainly originated from the PTE effect of $Cs_3Cu_2I_5$ film. The PTE photodetector arrays incorporated with large-area $Cs_3Cu_2I_5$ film also provide a successful application in flexible imaging. The results show that lead-free $Cs_3Cu_2I_5$ is a promising PTE material for fabricating a flexible and self-powered ultra-broadband photodetector and provide insight into the utility of metal halides in thermal-induced ultra-broadband photodetection.

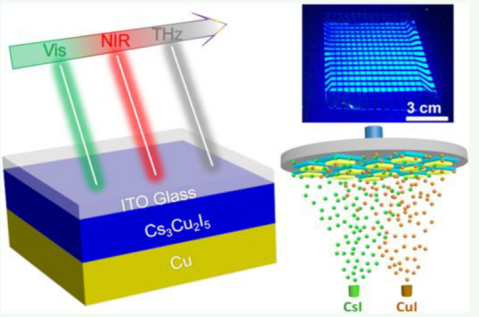

KEYWORDS: *photothermoelectric detector, $Cs_3Cu_2I_5$, ultra-broadband, teraherta, and lead-free perovskite*

1. INTRODUCTION

Ultra-broadband photodetectors for the ultraviolet (UV) and visible (vis) to terahertz (THz) range have attracted intensive attentions due to their great potentials for various applications, including optical communications, remote detection, photometers, security, and environmental monitoring.[1−8] However, current commercial ultra-broadband photodetectors cannot meet these demands of portable, versatile, low-cost utilities, and flexibility. For example, a bolometer must work at low temperatures (4 K) by being equipped with a cryogenic system,[9−11] and the Golay box exhibited a slow response time of a few hundred milliseconds.[12−14] In addition, owing to the limited band gaps of conventional semiconductors, ultra-broadband photodetection is mainly based on thermal sensing mechanisms such as pyroelectric, photothermoelectric (PTE), and bolometric effects, especially for mid-infrared (MIR), far-infrared (FIR), and THz detection.[15,16] The main challenge for the ultra-broadband photodetector capable of thermal sensing is the lack of suitable photoactive materials. Currently, many materials, including carbon materials,[17−20] black phosphorus,[21,22] metal dichalcogenides,[23] ferroelectric,[24] bismuthide,[25] and polytelluride,[26,27] have been used to fabricate ultra-broadband PTE detectors. However, for the complex fabrication processing of the PTE materials or devices, the needs for further flexible, large-scale, transparent, and wearable equipment applications are difficult to satisfy.

To date, extensive efforts have been devoted to fabricate flexible PTE detectors with ultra-broadband response. Among them, the PTE detectors made of topological insulators (such as SnTe,[28,29] Bi_2Te_3,[30] and SnSe[31]) have a high detectivity of $\sim 10^{10}$ cm $Hz^{1/2}$ W^{-1} and responsivity of ~4 mA W^{-1} under UV to the near infrared (NIR) spectrum. The flexible devices fabricated by transferring the epitaxial grown SnTe thin film onto a flexible substrate showed superior mechanical flexibility over hundreds of bending cycles.[28] Meanwhile, bismuth thin film grown from a chemical vapor deposition (CVD) technique has also been utilized to prepare a flexible PTE detector with the wavelength range from 405 to 1064 nm.[32] In addition, semiconductor polymers with merits of superior thermoelectric properties, low cost, feasible solution-processing, and mechanical flexibility,[33] such as poly(3,4-

Received: October 28, 2021
Accepted: January 6, 2022
Published: January 19, 2022

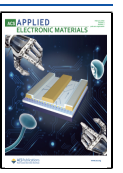

https://doi.org/10.1021/acsaelm.1c01060
ACS Appl. Electron. Mater. 2022, 4, 663−671

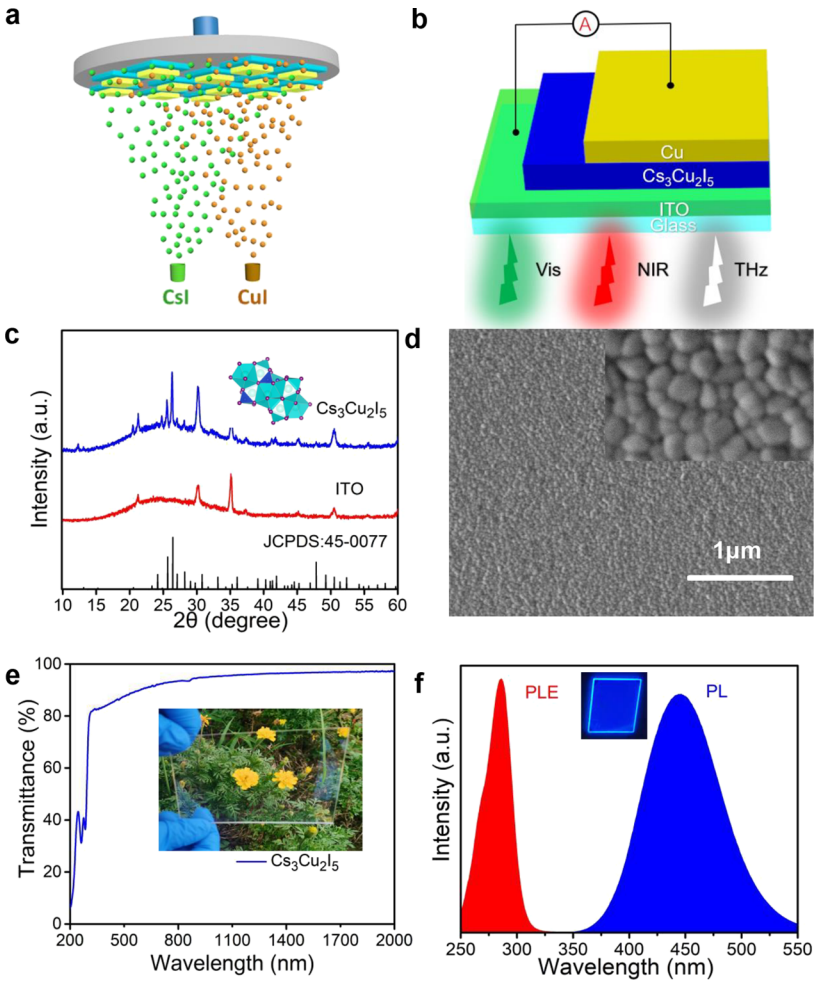

Figure 1. Schematic diagrams of (a) the dual-source co-evaporation deposition and (b) the photodetector incorporated with the $Cs_3Cu_2I_5$ thin film. (c) X-ray diffraction patterns of the $Cs_3Cu_2I_5$ thin film and ITO glass substrate. (d) SEM images and (e) transmittance spectra of the $Cs_3Cu_2I_5$ thin film. Illustration displaying yellow flowers visible to the naked eye through the $Cs_3Cu_2I_5$ thin film. (f) Photoluminescence excitation and emission spectra of the $Cs_3Cu_2I_5$ thin film. Inset image presenting a photograph of the $Cs_3Cu_2I_5$ thin film under UV light illumination.

ethylenedioxythiophene):poly(styrenesulfonate) (PEDOT:PSS), can also be applied to fabricate a flexible PTE detector. Self-powered MIR flexible photodetectors were fabricated by doping PEDOT:PSS films with graphene nanosheets, demonstrating a high photodetectivity of 1.4×10^7 cm $Hz^{1/2}$ W^{-1} despite a response time of seconds.[34] However, complex fabrication processing of topological materials,[27,35] hard adjustment of PEDOT:PSS/graphene composites,[33] and the requirement of new functionalitities[36,37] in the modern optoelectronic system are expected to develop novel materials for fabricating a flexible PTE detector with ultra-broadband response.

Metal halides are ideal photodetective materials to fabricate flexible and ultra-broadband detectors on account of a simple processing method, distinct optoelectronic properties and, potential PTE characteristics. Several reports have demonstrated that $CH_3NH_3PbI_3$ perovskite can be used to fabricate an ultra-broadband PTE photodetector.[38,39] High responsivities ranging from 10^5 to 10^2 mA W^{-1} are obtained within the UV−vis−THz wavelength and a rapid response time of nanoseconds.[38] However, lead toxicity in $CH_3NH_3PbI_3$ perovskites limits their wide application in ultra-broadband photodetectors. Therefore, it is necessary to explore lead-free metal halides for ultra-broadband photodetectors. In 2018, Jun et al. reported the $Cs_3Cu_2I_5$ with high PLQY, blue emission, and good air-stability.[40] Since then, emerging cuprous halides have received widespread attentions as a new type of optoelectronic material in UV photodetectors[41−44] and light-emitting diodes[45−48] owing to the advantages of non-toxicity, air-stablity, excellent optoelectronic characteristics, and a feasible fabrication process.[49,50] Furthermore, the prediction of high thermoelectric performance in the $Cs_3Cu_2I_5$ provides a potential application for PTE detectors.[51]

In the work, we prepare lead-free $Cs_3Cu_2I_5$ thin films using a dual-source co-evaporation deposition technique. The $Cs_3Cu_2I_5$ thin films exhibit superior optical transparency of over 80% ranging from 320 to 2000 nm. The devices fabricated by $Cs_3Cu_2I_5$ thin films demonstrate self-powered PTE photodetection from vis (532 nm) and NIR (980 nm) to THz (119 μm) at 0 bias voltage. The photodetectors exhibit a high responsivity of more than 1 mA W^{-1} and decent photodetectivity as high as $\sim 10^6$ cm $Hz^{1/2}$ W^{-1}. In addition, the demonstrated flexible photodetectors retain unchanged photoresponse characteristics under the bending of hundreds of times. The 15 × 15 photodetector array based on large-area $Cs_3Cu_2I_5$ film exhibits optical imaging capability.

https://doi.org/10.1021/acsaelm.1c01060
ACS Appl. Electron. Mater. 2022, 4, 663−671

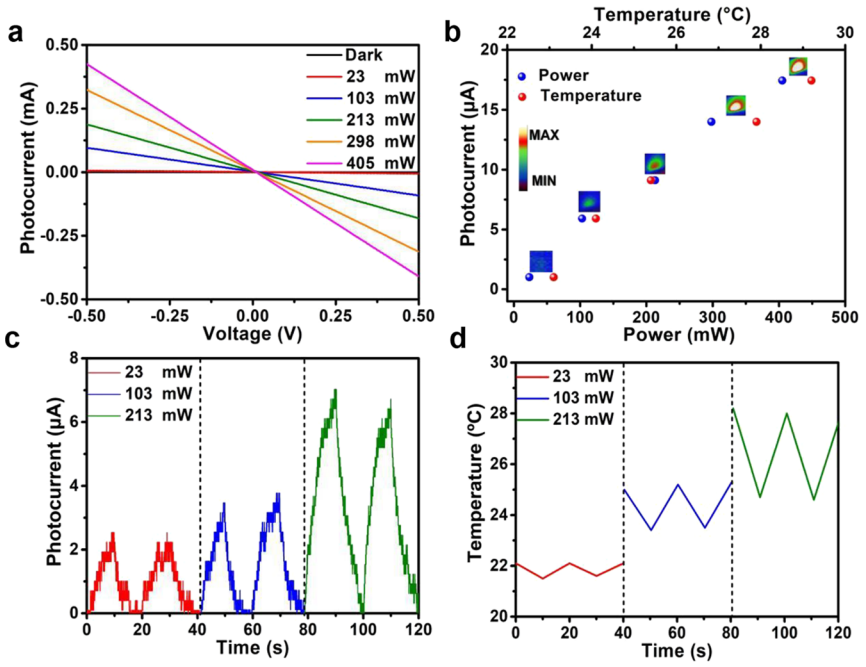

Figure 2. (a) Photocurrent−voltage (I−V) curves of the $Cs_3Cu_2I_5$ photodetector under the irradiation of a 980 nm laser with different powers. (b) Photocurrent as function of laser power and temperature in the photodetector under the laser irradiation. (c) Photocurrent−time (I−T) curves and (d) correspondent temperature changes (ΔT) of the working surface at the $Cs_3Cu_2I_5$ photodetector with energy powers of 23, 103, and 213 mW.

2. RESULTS AND DISCUSSION

The dual-source co-evaporation method was used to prepare $Cs_3Cu_2I_5$ films (Figure 1a). By controlling the evaporation rate of each component, the $Cs_3Cu_2I_5$ films can be deposited on the substrate in the vacuum system and the film thickness can be controlled, as shown in the experimental part. The X-ray diffraction (XRD) technique was utilized to determine the structure and crystallinity of the $Cs_3Cu_2I_5$ films. The XRD patterns of the $Cs_3Cu_2I_5$ films are shown in Figure 1c. In the diffraction patterns, diffraction peaks located at 24.80, 25.62, and 26.32°, corresponding to the crystal planes of (400), (312), and (222) of the $Cs_3Cu_2I_5$ films, respectively.[49] The $Cs_3Cu_2I_5$ thin films with an orthorhombic (Pnma) phase are in accordance with the above reported results, which indicates that CsI and CuI can be successfully transferred to the $Cs_3Cu_2I_5$ films by reasonably controlling the evaporation rate. The illustration in Figure 1c displays the crystallization structure of $Cs_3Cu_2I_5$. The $Cs_3Cu_2I_5$ exhibits a zero-dimensional structure phase, where CuI_4 tetrahedral units and CuI_3 trigonal units are edge-connected to form $[Cu_2I_5]^{3-}$ units separated by Cs^+ ions.[52] To elucidate the zero-dimensional structure, transmission electron microscopy (TEM) has been carried out in Figure S1 in the Supporting Information (SI).

Surface morphology of $Cs_3Cu_2I_5$ thin films prepared by the dual-source co-evaporation method was studied by scanning electron microscopy (SEM). The $Cs_3Cu_2I_5$ thin film possesses spherical and dispersed small crystals with full surface coverage (Figure 1d). The results of grain size distribution for the $Cs_3Cu_2I_5$ thin film are showed in Figure S2e in the SI. The $Cs_3Cu_2I_5$ thin film has average grain size of 73 ± 23 nm. The homogeneous and small grains are favorable for forming compact thin films, suppressing the dark current of the detector. In addition, the chemical composition and elemental distribution of the $Cs_3Cu_2I_5$ thin films were confirmed by energy-dispersive X-ray energy spectroscopy (EDX). As shown in Figure S2b−d in the SI, the atoms of Cu, Cs, and I are equally distributed in the $Cs_3Cu_2I_5$ thin film.

The light transparency range and band gap are significant properties for photoactive materials. Figure 1e shows the transmittance spectra of the $Cs_3Cu_2I_5$ thin films. We found that the $Cs_3Cu_2I_5$ thin films exhibit high transmittance over 80% with wavelength ranging from 320 to 2000 nm. The illustration in Figure 1e shows that yellow flowers could be clearly seen behind the large-area $Cs_3Cu_2I_5$ thin film. The results suggest that the $Cs_3Cu_2I_5$ thin film has potential for application in a highly transparent photodetector. In addition, the optical band gap of the $Cs_3Cu_2I_5$ thin film is estimated according to the relation:[53]

$$\beta d = \ln\left(\frac{1}{T}\right) \tag{1}$$

where T is the transmittance and d is the film thickness. Figure S3 in the SI displays the $(\beta E)^{1/2}$ versus $h\nu$ curve of the $Cs_3Cu_2I_5$ thin film, where β is the optical absorption coefficient and E is the photon energy. Therefore, the $Cs_3Cu_2I_5$ thin film shows an optical band gap of 3.9 eV in agreement with the band gap values of other reports.[45] Photoluminescence (PL) spectroscopy was used to rule out the existence of heterophase $CsCu_2I_3$ because of the obviously different PL spectra of $CsCu_2I_3$ and $Cs_3Cu_2I_5$. As shown in Figure 1f, as-grown $Cs_3Cu_2I_5$ thin films possess photoluminescence excitation (PLE) wavelength ranging from 250 to 320 nm and a PL peak at 450 nm, suggesting that the dual-source evaporation process do not form $CsCu_2I_3$ phase in the $Cs_3Cu_2I_5$ thin film due to the absence of the PL peak at 578 nm.

The photoresponse characteristics of the $Cs_3Cu_2I_5$ thin films fabricated with dual-source co-evaporation were studied through a vertically integrated device structure of ITO/$Cs_3Cu_2I_5$/Cu. In the device, indium tin oxide (ITO) acts as the electrode, the $Cs_3Cu_2I_5$ thin film acts as a photoactive material, and copper (Cu) acts as another electrode. Figure 1b depicts

https://doi.org/10.1021/acsaelm.1c01060
ACS Appl. Electron. Mater. 2022, 4, 663−671

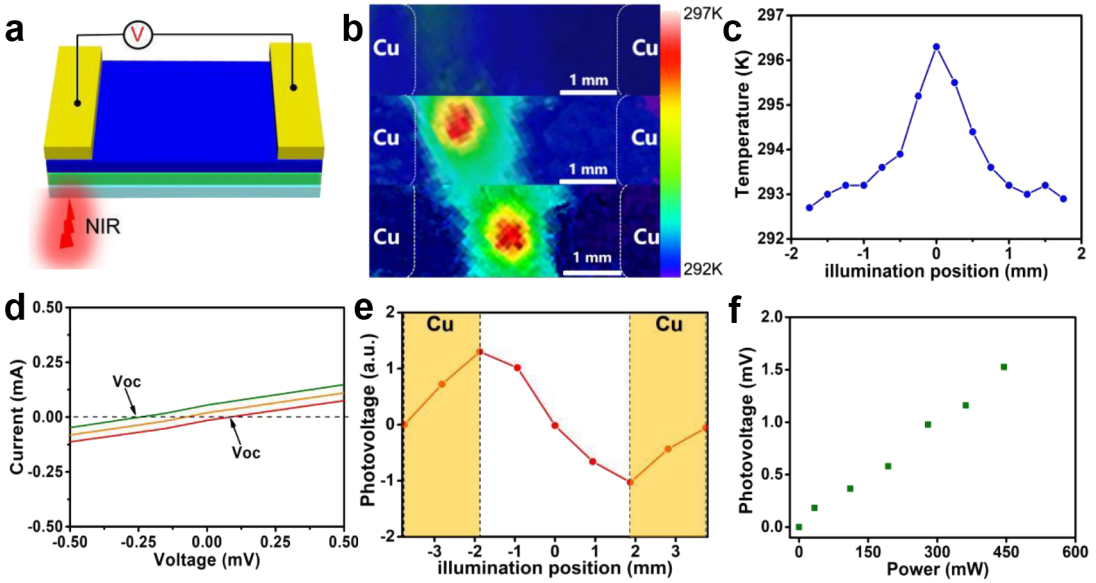

Figure 3. (a) Schematic diagram of the $Cs_3Cu_2I_5$ photodetector. (b) Temperature distribution of the $Cs_3Cu_2I_5$ detector irradiated with a 980 nm laser beam at the $Cs_3Cu_2I_5$ channel between two parallel electrodes. (c) Temperature profile extracted along two parallel electrodes in (b). The dots are actual measurements. (d) Current−voltage (I−V) characteristics of the $Cs_3Cu_2I_5$ detector in the dark and under the irradiation of laser on the positive and negative end. (e) Photogenerated potentials corresponding to the position of moving laser spot between two parallel electrodes under the laser irradiation. (f) Photovoltage as a function of light power in the $Cs_3Cu_2I_5$ detector.

the schematic diagram of the photodetector. The photocurrent versus voltage (I−V) curves were obtained from the photodetectors under illumination by a 980 nm (NIR) laser at different laser powers, and the results are shown as in Figure 2a. I−V curves both have linear characteristics, indicating weak Schottky barriers between the ITO or Cu electrode and the $Cs_3Cu_2I_5$ thin films.[54] The weak Schottky barrier is attributed to the band bending between Cu and $Cs_3Cu_2I_5$ (Figure S4). Figure 2b exhibits the relationship between photocurrent and laser power. The photocurrents increase gradually from 1.01 to 17.43 μA as the light intensity increases from 23 to 405 mW. The photocurrents with 0 V bias are proportional to the laser powers, which indicates that the devices can accurately differentiate incident light intensities as a kind of self-power.

To further investigate the photoresponse of the $Cs_3Cu_2I_5$ photodetector, the responsivity (R) and the specific detectivity (D^*) were estimated from the I−V curves. The R can be calculated by the equation:[39]

$$R = \frac{I_{ph}}{P} = \frac{I_{illu} - I_{dark}}{P} \quad (2)$$

where I_{ph} is the photocurrent, P is the incident power, I_{illu} is the current of the illuminated device, and I_{dark} is the current of the device in the dark. The maximum R value of the $Cs_3Cu_2I_5$ photodetector is 1.1 mA W^{-1}. The D^* is calculated by the following equation:[38]

$$D^* = \frac{R\sqrt{S}}{\sqrt{2eI_{dark}}} \quad (3)$$

where e is the electron charge and S is the active area of the device. Figure S5 in the SI shows the D^* curve of the $Cs_3Cu_2I_5$ photodetector as a function of voltage. The maximum D^* value of 6.5 × 10^6 cm $Hz^{1/2}$ W^{-1} was obtained from the $Cs_3Cu_2I_5$ photodetector.

The photocurrent generation mechanism of the photodetectors incorporated with the $Cs_3Cu_2I_5$ thin films will be discussed here to reveal the underlying photophysics. Generally, the photodetectors based on the photoconductive (PC) or photovoltaic (PV) effect only realize the light detection wavelength, in which the photon energies are larger than the band gap of the photoactive material.[55] According to the obtained band gap of the $Cs_3Cu_2I_5$ thin films, PC and PV mechanisms cannot be applied to explain the photoresponse of the $Cs_3Cu_2I_5$ photodetector. Apart from the above two photocurrent generation mechanisms, the thermal-induced photoresponse mechanism including bolometric, pyroelectric, and PTE effects may be responsible for the photocurrent generation of the $Cs_3Cu_2I_5$ photodetector.[15] To study the thermal-induced photoresponse mechanism, the temperature variations of the devices were tested under the periodical illumination (Figure 2b). In addition, the time-dependent rise and fall of temperature on the surface of the devices were generated by repeatedly controlling the light switch (Figure 2d), indicating that the devices possess thermal switching behaviors under on/off illumination switch. The light was off within the first 10 s of the initial test. When the laser is turned on, the surface temperature of the device increases and a corresponding reduced photocurrent for the device (Figure 2c). However, the surface temperature of the device decreases, resulting in an increase in the photocurrent when the laser is turned off. In addition, the surface temperature change (ΔT) of the devices is enhanced when increasing the power of lasers (Figure 2c,d). The results demonstrate that the photocurrent generation of the $Cs_3Cu_2I_5$ photodetector is closely related to the photoinduced temperature variations on the surface of the photodetector. In the thermal-induced photoresponse mechanism, bolometric devices usually operate by biasing the bolometer with a voltage or current.[16] Therefore, the bolometric effect cannot explain photocurrent generation in the $Cs_3Cu_2I_5$ photodetector due to the photoresponse behaviors of the $Cs_3Cu_2I_5$ photodetector at zero biasing. Also, the pyroelectric effect can be ruled out according to the time-dependent photoresponse behaviors obtained from the

https://doi.org/10.1021/acsaelm.1c01060
ACS Appl. Electron. Mater. 2022, 4, 663−671

devices under laser irradiation,[56−59] as shown in Figure S6 in the SI. Therefore, the PTE mechanism is responsible for the photocurrent generation.

To further reveal the PTE response mechanism in our fabricated device, a lateral device with two parallel electrodes was fabricated to illustrate the PTE effect in the $Cs_3Cu_2I_5$ photodetector. The schematic diagram of the device is shown in Figure 3a. Temperature distribution and difference of the devices were tested under 980 nm laser illumination using an infrared imaging device. To exclude the influence of the metal electrode, we measured temperature distribution by recording thermal image at the center or edge of the $Cs_3Cu_2I_5$ channel rather than the contact area. Figure 3b shows the temperature distribution over the devices with a focused laser beam at the center of the $Cs_3Cu_2I_5$ channel and the edge of $Cs_3Cu_2I_5$−metal contact. Figure 3b also exhibits that our system can establish a stable temperature difference between two parallel electrodes. In addition, Figure 3c shows temperature profile extracted along the horizontal central axis of the $Cs_3Cu_2I_5$ channel imaging in Figure 3b. Thus, the ΔT between the two electrodes is 3.3 K when illuminating at one electrode.

Figure 3d presents the $I-V$ curves at alternate connection between positive and negative electrodes of the devices under dark conditions and laser illumination. The quasi-linear behaviors indicate that the $Cs_3Cu_2I_5$ thin films have a weak Schottky barrier with the Cu electrodes. When the laser beam illuminates on the $Cs_3Cu_2I_5$−metal contact at both ends, the $I-V$ curve is moving in the opposite direction. The device exhibits an open-circuit voltage (V_{OC}) of 167 μV under illumination, indicating a typical PTE behavior.[25] For the PTE model, local laser irradiation can induce a ΔT at both terminals of the channel layer. The temperature gradient produces a built-in electrical field with the direction from the high-temperature terminal to the low-temperature terminal. Thus, the charge carriers are driven by a built-in electrical field in the $Cs_3Cu_2I_5$ channel layer, which generates a current.[31] According to the above obtained Voc = 167 μV and ΔT = 3.3 K, the Seebeck coefficient S = Voc/ΔT = 50.6 μV/K was obtained for the $Cs_3Cu_2I_5$ film at room temperature.[28] The obtained Seebeck coefficient of the $Cs_3Cu_2I_5$ thin film is consistent with that from its thermoelectric simulations.[51] To shed more light on the thermoelectric performance, the scanning photovoltage of the device was measured by mechanically scanning the laser spot along the $Cs_3Cu_2I_5$ channel between both electrodes. As shown in Figure 3e, a sharp increase or decrease was observed near to the $Cs_3Cu_2I_5$−metal interface. The results are closely correlated with PTE characteristics. When the laser irradiates the $Cs_3Cu_2I_5$−Cu interface, the temperature distribution between the two electrodes shows obvious asymmetry. The strongest interface asymmetry produces a sharp increase and decrease of photovoltage near to the $Cs_3Cu_2I_5$−Cu interface. Figure 3f shows photovoltage as a function of laser power in the $Cs_3Cu_2I_5$ photodectector under the laser illumination. The photothermal conversion between the incident light and $Cs_3Cu_2I_5$ thin films is enhanced by the increase of laser power, generating the enhanced ΔT between the two terminals of the device. The enhanced ΔT between two electrodes induces an increase in the built-in electric field based on the thermoelectric Seebeck effect.[28]

Owing to its low-temperature processing, the $Cs_3Cu_2I_5$ thin film is considered as a good candidate material for fabrication of flexible devices. Thus, a flexible photodetector with a structure of PEN/ITO/$Cs_3Cu_2I_5$/Cu was fabricated. The incident laser was used to obtain time-dependent photoresponse curves of the devices after several bending cycles. A bending cycle is regarded as bending from the plane to the curved state, where the device is bent with a diameter of 1.1 cm (Figure 4a,b), and then back to the plane state. The device

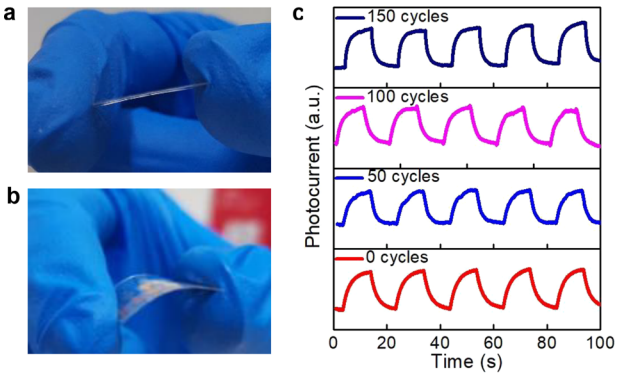

Figure 4. Photographs of the $Cs_3Cu_2I_5$ flexible photodetector at (a) a flat condition and (b) a curving condition. (c) Photocurrent versus time curves of the flexible $Cs_3Cu_2I_5$ photodetector after bending 0, 50, 100, and 150 times under the laser irradiation.

can still work stably even after 150 bending cycles (Figure 4c). The photoresponse characteristics do not change significantly, indicating that the devices exhibit excellent robustness and flexibility. In addition, the flexibility of the $Cs_3Cu_2I_5$ photodetector provides potential for further application in flexible sensor arrays.

The dual-source co-evaporation technique provides great potential for fabricating large-area photodetector arrays. We fabricated 15 × 15 photodetector arrays on the flexible PET substrate to explore light imaging capabilities. Figure 5a,b shows the photographs of the Au/$Cs_3Cu_2I_5$/Au photodetector arrays under UV illumination and bending condition. As schematically shown in Figure 5c, a home-made mask with a "T" pattern moving in the X and Y directions was placed between the Au/$Cs_3Cu_2I_5$/Au photodetector arrays and illuminating laser, and the electrical signal record system was employed to record the photocurrent. Figure 5d demonstrates the photocurrent on each pixel of the photodetector arrays under the mask with the letter T. It should be noted that the letter T is clearly visible in Figure 5d, indicating the light imaging capability of the Au/$Cs_3Cu_2I_5$/Au photodetector arrays.

In order to extend the light response range of the $Cs_3Cu_2I_5$ photodetector from NIR to vis or THz, the light detection performance of the $Cs_3Cu_2I_5$ photodetector under laser irradiation of 532 nm (vis) and 119 μm (THz) was studied. The $I-V$ curves were obtained from the $Cs_3Cu_2I_5$ photodetector under illumination by 532 nm and 119 μm lasers at a variety of laser powers, and the results are shown as in Figure S7a,b in the SI. Figure 6a,b exhibits the relationship between photocurrent, surface temperature, and laser power at two tested wavelengths. Under illumination with 532 nm and 119 μm lasers, the photocurrent and temperature of the $Cs_3Cu_2I_5$ photodetector increase gradually as the light intensities of the lasers increase. The maximum R values of the devices are calculated to be 49.2 and 3.7 mA W^{-1}, and the maximum D^* values are 8.2 × 10^7 and 6.4 × 10^6 cm $Hz^{1/2}$ W^{-1}, under illumination with 532 nm and 119 μm lasers, respectively. The results are comparable to representative photodetectors based

https://doi.org/10.1021/acsaelm.1c01060
ACS Appl. Electron. Mater. 2022, 4, 663−671

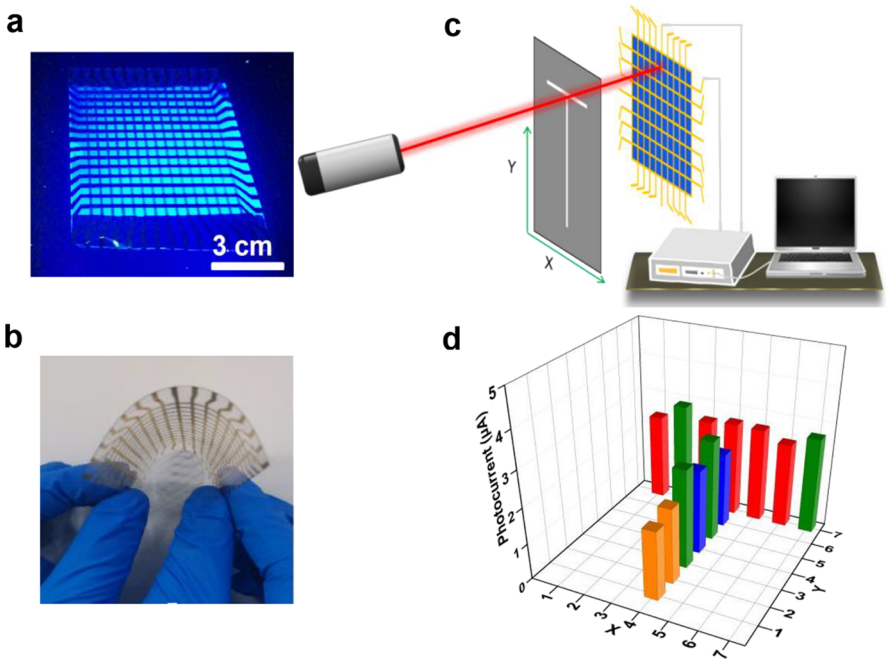

Figure 5. (a) Photograph of flexible photodetector arrays under the UV light illumination. (b) Photograph of the flexible photodetector arrays after bending. (c) Sketch diagram of the sensing process of the Au/$Cs_3Cu_2I_5$/Au flexible photodetector arrays under the irradiation of a 980 nm laser. (d) A three-dimensional diagram shows the photocurrent on each pixel of the photodetector arrays.

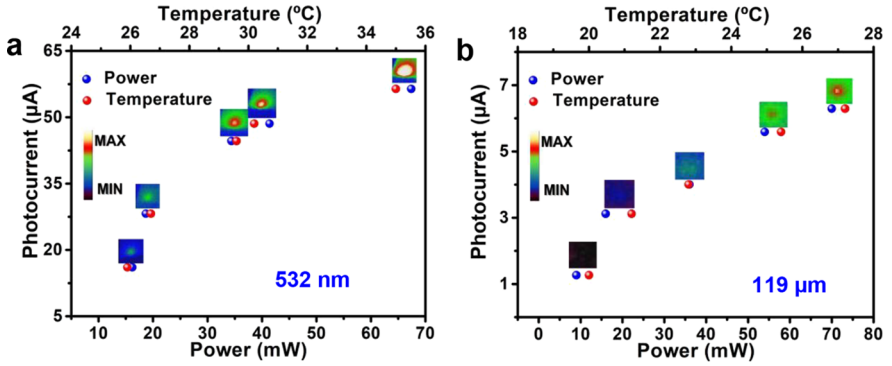

Figure 6. Photocurrent as function of laser power and temperature in the photodetector under the irradiation of (a) 532 nm and (b) 119 μm lasers.

on the PTE mechanism. The comparison between this work and the reported PTE-based photodetectors is shown in Table S1. In addition, the $Cs_3Cu_2I_5$ photodetector possesses thermal switching behaviors under on/off illumination switch and further resulting in photocurrent switching (Figure S8a,S8b), which indicates that the devices incorporated with the $Cs_3Cu_2I_5$ thin films can achieve ultra-broadband photodetection from vis to NIR to THz.

3. CONCLUSIONS

In summary, we reported an ultra-broadband PTE detector based on the lead-free $Cs_3Cu_2I_5$ thin film. The $Cs_3Cu_2I_5$ thin film was prepared using a dual-source co-evaporation deposition. A combination characterization of XRD patterns, SEM images, transmittance, and PL spectroscopies was conducted to study the composition, surface morphology, and spectra properties of the $Cs_3Cu_2I_5$ thin films. Furthermore, the photodetectors incorporated with the $Cs_3Cu_2I_5$ thin films exhibit a self-powered ultra-broadband photoresponse wavelength range from vis (532 nm) to NIR (980 nm) to THz (119 μm). Under 532 nm, 980 nm, and 119 μm laser irradiation, the maximum R values of the devices are 49.2, 1.1, and 3.7 mA W^{-1}, respectively. The flexible photodetector incorporated with the $Cs_3Cu_2I_5$ thin film still works stably even after 150 bending cycles. 15 × 15 photodetector arrays on the flexible substrate exhibit light imaging capabilities. These results demonstrate that the work provides a promising PTE material for the ultra-broadband flexible photodetector.

4. EXPERIMENTAL SECTION

4.1. Materials. Cuprous iodide (99.999%), cesium iodide (99.998%), and copper particles (99.9%) were purchased from Alfa-Aesar. Indium tin oxide (ITO) conductive glass and ITO PET substrate (Peccell) were purchased from Advanced Election Technology Corp., Ltd. All materials are used as received without further purification.

4.2. Fabrication of Films. The $Cs_3Cu_2I_5$ film was prepared by a dual-source co-evaporated method similarly to our previously published method.[60] The evaporation rates of CuI and CsI were 1 and 2 A/s, respectively.

4.3. Characterization of Films. X-ray diffraction (XRD) patterns of the $Cs_3Cu_2I_5$ films were characterized on Rigaku SmartLab. Transmittance spectra of the $Cs_3Cu_2I_5$ films were tested on a

https://doi.org/10.1021/acsaelm.1c01060
ACS Appl. Electron. Mater. 2022, 4, 663−671

SHIMADZU SolidSpec-3700 spectrophotometer. Energy dispersive X-ray energy spectroscopy (EDX) and scanning electron microscopy (SEM) images of the $Cs_3Cu_2I_5$ films were measured on an Apreo S LoVac. The thickness of the $Cs_3Cu_2I_5$ films was measured on a surface profilometer (Bruker, Dektak XT). Photoluminescence excitation (PLE) and photoluminescence (PL) spectroscopy were obtained on a HORIBA QM 8000 fluorescence spectrophotometer.

4.4. Fabrication of Devices. The $Cs_3Cu_2I_5$ thin film (200 nm) was prepared atop the pre-cleaned ITO glass substrates or PET substrate. Afterward, in the vacuum, a copper film of about 100 nm was deposited by thermal evaporation on the top of the $Cs_3Cu_2I_5$ film under a pressure of 2×10^{-6} mbar. For the vertical device, the effective area of mask is 0.16 cm^2. The distance between the two parallel electrodes is 4 mm in the lateral device, and the size of each electrode is 1.5 × 7 mm.

4.5. Characterization of Devices. *I*–*V* characteristics of the photodetectors were measured using a Keithley 2400 source meter under 532 nm (MGL-III-532, Changchun New Industries Ltd.), 980 nm (FC-980, Changchun New Industries Ltd.), and 119 μm (FLIR 100, Edinburgh Instruments Ltd.) laser illumination. Light powers of 532 and 980 nm were calibrated using a power meter with an RS232 port (Ophir NOVA II). The light power of the 119 μm THz laser was calibrated using a Golay cell (GC-1P, Tydex Ltd). The temperature images of the photodetectors were tested using an infrared imaging device (HIKVISION H13). The on/off switching behaviors of the photodetectors were measured using potentiostatic and galvanostatic instrument (Metrohm Autolab PGSTAT204).

■ ASSOCIATED CONTENT

Supporting Information

The Supporting Information is available free of charge at https://pubs.acs.org/doi/10.1021/acsaelm.1c01060.

TEM, SEM images and EDX data of the $Cs_3Cu_2I_5$ film; statistics of grain size distribution for the $Cs_3Cu_2I_5$ film; plot of $(\beta E)^{1/2}$ against E for the $Cs_3Cu_2I_5$ film; schematic diagram of band bending between Cu and $Cs_3Cu_2I_5$; D^* of the $Cs_3Cu_2I_5$ photodetector; photoelectric response characteristics and photocurrent switching of the $Cs_3Cu_2I_5$ photodetector under the irradiation of 532 nm and 119 μm lasers; and comparison between this report and reported PTE detectors (PDF)

■ AUTHOR INFORMATION

Corresponding Authors

Xiang Yao − *Institute of Molecular Plus, Tianjin University, Tianjin 300072, P. R. China;* orcid.org/0000-0003-3290-8702; Email: yaoxiang@tju.edu.cn

Minglie Hu − *Ultrafast Laser Laboratory, Key Laboratory of Opto-electronic Information Science and Technology of Ministry of Education, College of Precision Instruments and Opto-electronics Engineering, Tianjin University, Tianjin 300072, China*; Email: huminglie@tju.edu.cn

Authors

Yunzhi Gu − *Ultrafast Laser Laboratory, Key Laboratory of Opto-electronic Information Science and Technology of Ministry of Education, College of Precision Instruments and Opto-electronics Engineering, Tianjin University, Tianjin 300072, China*

Huaxiu Geng − *Institute of Molecular Plus, Tianjin University, Tianjin 300072, P. R. China*

Mengying Long − *Key Laboratory for Green Chemical Technology of Ministry of Education, School of Chemical Engineering and Technology, Tianjin University, Tianjin 300072, China*

Guijian Guan − *Institute of Molecular Plus, Tianjin University, Tianjin 300072, P. R. China*

Mingyong Han − *Institute of Molecular Plus, Tianjin University, Tianjin 300072, P. R. China; Institute of Materials Research and Engineering, Singapore 138634;* orcid.org/0000-0002-7519-6779

Complete contact information is available at: https://pubs.acs.org/10.1021/acsaelm.1c01060

Author Contributions

#Y.G. and X. Y. contributed equally to this work.

Notes

The authors declare no competing financial interest.

■ ACKNOWLEDGMENTS

This work was supported by the National Natural Science Foundation of China (52001225).

■ REFERENCES

(1) Liu, H.; Zhong, H.; Karpowicz, N.; Chen, Y.; Zhang, X. Terahertz Spectroscopy and Imaging for Defense and Security Applications. *Proc. IEEE* **2007**, *95*, 1514−1527.

(2) Michael, C. K.; Taday, P. F.; Bryan, E. C.; Cluff, J. A.; Anthony, J. F.; William, R. T. In Security applications of terahertz technology. *Proc. SPIE* **2003**, *5070*, 44.

(3) Niu, Y.; Li, Y.; Jin, D.; Su, L.; Vasilakos, A. V. A survey of millimeter wave communications (mmWave) for 5G: opportunities and challenges. *Wireless Networks* **2015**, *21*, 2657−2676.

(4) Pickwell, E.; Wallace, V. P. Biomedical applications of terahertz technology. *J. Phys. D: Appl. Phys.* **2006**, *39*, R301−R310.

(5) Vincent, P. W.; Emma, M.; Anthony, J. F.; Thomas, L.; Elena, P.; Sarah, P.; Anand, P. Terahertz pulsed imaging and spectroscopy of breast tumors, *Optical Methods in the Life Sciences*; International Society for Optics and Photonics: 2006.

(6) Xu, W.; Guo, Y.; Zhang, X.; Zheng, L.; Zhu, T.; Zhao, D.; Hu, W.; Gong, X. Room-Temperature-Operated Ultrasensitive Broadband Photodetectors by Perovskite Incorporated with Conjugated Polymer and Single-Wall Carbon Nanotubes. *Adv. Funct. Mater.* **2018**, *28*, 1705541.

(7) Zhu, T.; Zheng, L.; Yao, X.; Liu, L.; Huang, F.; Cao, Y.; Gong, X. Ultrasensitive Solution-Processed Broadband PbSe Photodetectors through Photomultiplication Effect. *ACS Appl. Mater. Interfaces* **2019**, *11*, 9205−9212.

(8) Xin, B.; Pak, Y.; Mitra, S.; Almalawi, D.; Alwadai, N.; Zhang, Y.; Roqan, I. S. Self-Patterned $CsPbBr_3$ Nanocrystals for High-Performance Optoelectronics. *ACS Appl. Mater. Interfaces* **2019**, *11*, 5223−5231.

(9) Langley, S. P. The Bolometer and Radiant Energy. *Proceedings of the American Academy of Arts and Sciences* **1880**, *16*, 342−358.

(10) Chi-Anh, N.; Shin, H.-J.; Kim, K. T.; Han, Y.-H.; Moon, S. Characterization of uncooled bolometer with vanadium tungsten oxide infrared active layer. *Sens. Actuators, A* **2005**, *123*, 87−91.

(11) Wu, Y.; Qu, Z.; Osman, A.; Cao, W.; Khokhar, A. Z.; Soler Penades, J.; Muskens, O. L.; Mashanovich, G. Z.; Nedeljkovic, M. Mid-Infrared Nanometallic Antenna Assisted Silicon Waveguide Based Bolometers. *ACS Photonics* **2019**, *6*, 3253−3260.

(12) Dall'Oglio, G.; Melchiorri, B.; Melchiorri, F.; Natale, V. Comparison between carbon, silicon and germanium bolometers and Golay cell in the far infrared. *Infrared Phys.* **1974**, *14*, 347−350.

(13) Vavrouch, D.; Boček, V. Some optimum parameters of golay detector of infra-red radiation. *Cechoslovackij fiziceskij zurnal B* **1963**, *13*, 459−470.

(14) Yamashita, K.; Murata, A.; Okuyama, M. Miniaturized infrared sensor using silicon diaphragm based on Golay cell. *Sens. Actuators, A* **1998**, *66*, 29−32.

(15) Lu, X.; Sun, L.; Jiang, P.; Bao, X. Progress of Photodetectors Based on the Photothermoelectric Effect. *Adv. Mater.* **2019**, *31*, 1902044.
(16) Stewart, J. W.; Wilson, N. C.; Mikkelsen, M. H. Nanophotonic Engineering: A New Paradigm for Spectrally Sensitive Thermal Photodetectors. *ACS Photonics* **2021**, *8*, 71−84.
(17) Yang, H.; Cao, Y.; He, J.; Zhang, Y.; Jin, B.; Sun, J.-L.; Wang, Y.; Zhao, Z. Highly conductive free-standing reduced graphene oxide thin films for fast photoelectric devices. *Carbon* **2017**, *115*, 561−570.
(18) Cao, Y.; Zhu, J.; Xu, J.; He, J.; Sun, J.-L.; Wang, Y.; Zhao, Z. Ultra-Broadband Photodetector for the Visible to Terahertz Range by Self-Assembling Reduced Graphene Oxide-Silicon Nanowire Array Heterojunctions. *Small* **2014**, *10*, 2345−2351.
(19) Deng, T.; Zhang, Z.; Liu, Y.; Wang, Y.; Su, F.; Li, S.; Zhang, Y.; Li, H.; Chen, H.; Zhao, Z.; Li, Y.; Liu, Z. Three-Dimensional Graphene Field-Effect Transistors as High-Performance Photodetectors. *Nano Lett.* **2019**, *19*, 1494−1503.
(20) Cai, X.; Sushkov, A. B.; Suess, R. J.; Jadidi, M. M.; Jenkins, G. S.; Nyakiti, L. O.; Myers-Ward, R. L.; Li, S.; Yan, J.; Gaskill, D. K.; Murphy, T. E.; Drew, H. D.; Fuhrer, M. S. Sensitive room-temperature terahertz detection via the photothermoelectric effect in graphene. *Nat. Nanotechnol.* **2014**, *9*, 814−819.
(21) Viti, L.; Hu, J.; Coquillat, D.; Knap, W.; Tredicucci, A.; Politano, A.; Vitiello, M. S. Black Phosphorus Terahertz Photodetectors. *Adv. Mater.* **2015**, *27*, 5567−5572.
(22) Xu, Y.; Liu, C.; Guo, C.; Yu, Q.; Guo, W.; Lu, W.; Chen, X.; Wang, L.; Zhang, K. High performance near infrared photodetector based on in-plane black phosphorus p-n homojunction. *Nano Energy* **2020**, *70*, 104518.
(23) Xie, Y.; Liang, F.; Chi, S.; Wang, D.; Zhong, K.; Yu, H.; Zhang, H.; Chen, Y.; Wang, J. Defect Engineering of MoS_2 for Room-Temperature Terahertz Photodetection. *ACS Appl. Mater. Interfaces* **2020**, *12*, 7351−7357.
(24) Fang, H.; Xu, C.; Ding, J.; Li, Q.; Sun, J.-L.; Dai, J.-Y.; Ren, T.-L.; Yan, Q. Self-Powered Ultrabroadband Photodetector Monolithically Integrated on a PMN−PT Ferroelectric Single Crystal. *ACS Appl. Mater. Interfaces* **2016**, *8*, 32934−32939.
(25) Wang, Y.; Niu, Y.; Chen, M.; Wen, J.; Wu, W.; Jin, Y.; Wu, D.; Zhao, Z. Ultrabroadband, Sensitive, and Fast Photodetection with Needle-Like $EuBiSe_3$ Single Crystal. *ACS Photonics* **2019**, *6*, 895−903.
(26) Yao, J.; Shao, J.; Wang, Y.; Zhao, Z.; Yang, G. Ultra-broadband and high response of the Bi2Te3−Si heterojunction and its application as a photodetector at room temperature in harsh working environments. *Nanoscale* **2015**, *7*, 12535−12541.
(27) Makino, K.; Kuromiya, S.; Takano, K.; Kato, K.; Nakajima, M.; Saito, Y.; Tominaga, J.; Iida, H.; Kinoshita, M.; Nakano, T. THz Pulse Detection by Multilayered GeTe/Sb2Te3. *ACS Appl. Mater. Interfaces* **2016**, *8*, 32408−32413.
(28) Liu, H.; Liu, Y.; Dong, S.; Xu, H.; Wu, Y.; Hao, L.; Cao, B.; Li, M.; Wang, Z.; Han, Z.; Yan, K. Photothermoelectric SnTe Photodetector with Broad Spectral Response and High On/Off Ratio. *ACS Appl. Mater. Interfaces* **2020**, *12*, 49830−49839.
(29) Yang, J.; Yu, W.; Pan, Z.; Yu, Q.; Yin, Q.; Guo, L.; Zhao, Y.; Sun, T.; Bao, Q.; Zhang, K. Ultra-Broadband Flexible Photodetector Based on Topological Crystalline Insulator SnTe with High Responsivity. *Small* **2018**, *14*, 1802598.
(30) Yao, J.; Zheng, Z.; Yang, G. All-Layered 2D Optoelectronics: A High-Performance UV−vis−NIR Broadband SnSe Photodetector with Bi_2Te_3 Topological Insulator Electrodes. *Adv. Funct. Mater.* **2017**, *27*, 1701823.
(31) Zhong, Y.; Zhang, L.; Linseis, V.; Qin, B.; Chen, W.; Zhao, L.-D.; Zhu, H. High-quality textured SnSe thin films for self-powered, rapid-response photothermoelectric application. *Nano Energy* **2020**, *72*, 104742.
(32) Zhou, Q.; Lu, D.; Tang, H.; Luo, S.; Li, Z.; Li, H.; Qi, X.; Zhong, J. Self-Powered Ultra-Broadband and Flexible Photodetectors Based on the Bismuth Films by Vapor Deposition. *ACS Appl. Electron. Mater.* **2020**, *2*, 1254−1262.
(33) Huang, D.; Zou, Y.; Jiao, F.; Zhang, F.; Zang, Y.; Di, C.-a.; Xu, W.; Zhu, D. Interface-Located Photothermoelectric Effect of Organic Thermoelectric Materials in Enabling NIR Detection. *ACS Appl. Mater. Interfaces* **2015**, *7*, 8968−8973.
(34) Zhang, M.; Yeow, J. T. W. A flexible, scalable, and self-powered mid-infrared detector based on transparent PEDOT: PSS/graphene composite. *Carbon* **2020**, *156*, 339−345.
(35) Wang, F.; Li, L.; Huang, W.; Li, L.; Jin, B.; Li, H.; Zhai, T. Submillimeter 2D Bi_2Se_3 Flakes toward High-Performance Infrared Photodetection at Optical Communication Wavelength. *Adv. Funct. Mater.* **2018**, *28*, 1802707.
(36) Kim, H.; Ahn, J.-H. Graphene for flexible and wearable device applications. *Carbon* **2017**, *120*, 244−257.
(37) Niu, Y.; Wang, Y.; Wu, W.; Wang, P.; Sun, J.; Wen, J.; Lu, X.; Jiang, P.; Zhang, S.; Wang, N.; Wu, D.; Zhao, Z. Ultrabroadband, Fast, and Flexible Photodetector Based on $HfTe_5$ Crystal. *Adv. Opt. Mater.* **2020**, *8*, 2000833.
(38) Li, Y.; Zhang, Y.; Li, T.; Li, M.; Chen, Z.; Li, Q.; Zhao, H.; Sheng, Q.; Shi, W.; Yao, J. Ultrabroadband, Ultraviolet to Terahertz, and High Sensitivity $CH_3NH_3PbI_3$ Perovskite Photodetectors. *Nano Lett.* **2020**, *20*, 5646−5654.
(39) Li, Y.; Zhang, Y.; Li, T.; Tang, X.; Li, M.; Chen, Z.; Li, Q.; Sheng, Q.; Shi, W.; Yao, J. A fast response, self-powered and room temperature near infrared-terahertz photodetector based on a MAPbI3/PEDOT:PSS composite. *J. Mater. Chem. C* **2020**, *8*, 12148−12154.
(40) Jun, T.; Sim, K.; Iimura, S.; Sasase, M.; Kamioka, H.; Kim, J.; Hosono, H. Lead-free highly efficient blue-emitting Cs3Cu2I5 with 0D electronic structure. *Adv. Mater.* **2018**, *30*, 1804547.
(41) Li, Y.; Shi, Z.; Wang, L.; Chen, Y.; Liang, W.; Wu, D.; Li, X.; Zhang, Y.; Shan, C.; Fang, X. Solution-processed one-dimensional $CsCu_2I_3$ nanowires for polarization-sensitive and flexible ultraviolet photodetectors. *Mater. Horiz.* **2020**, *7*, 1613−1622.
(42) Li, Z.; Li, Z.; Shi, Z.; Fang, X. Facet-Dependent, Fast Response, and Broadband Photodetector Based on Highly Stable All-Inorganic $CsCu_2I_3$ Single Crystal with 1D Electronic Structure. *Adv. Funct. Mater.* **2020**, *30*, 2002634.
(43) Liang, Y.; Xie, C.; Dong, C.-y.; Tong, X.-w.; Yang, W.-h.; Wu, C.-y.; Luo, L.-b. Electrically adjusted deep-ultraviolet/near-infrared single-band/dual-band imaging photodetectors based on $Cs_3Cu_2I_5$/$PdTe_2$/Ge multiheterostructures. *J. Mater. Chem. C* **2021**, 14897.
(44) Liang, W.; Wang, L.; Li, Y.; Zhang, F.; Chen, X.; Wu, D.; Tian, Y.; Li, X.; Shan, C.; Shi, Z. Stable and ultraviolet-enhanced broadband photodetectors based on Si nanowire arrays-Cs3Cu2I5 nanocrystals hybrid structures. *Materials Today Physics* **2021**, *18*, 100398.
(45) Wang, L.; Shi, Z.; Ma, Z.; Yang, D.; Zhang, F.; Ji, X.; Wang, M.; Chen, X.; Na, G.; Chen, S.; Wu, D.; Zhang, Y.; Li, X.; Zhang, L.; Shan, C. Colloidal Synthesis of Ternary Copper Halide Nanocrystals for High-Efficiency Deep-Blue Light-Emitting Diodes with a Half-Lifetime above 100 h. *Nano Lett.* **2020**, *20*, 3568−3576.
(46) Chen, H.; Pina, J. M.; Yuan, F.; Johnston, A.; Ma, D.; Chen, B.; Li, Z.; Dumont, A.; Li, X.; Liu, Y.; Hoogland, S.; Zajacz, Z.; Lu, Z.; Sargent, E. H. Multiple Self-Trapped Emissions in the Lead-Free Halide Cs3Cu2I5. *The Journal of Physical Chemistry Letters* **2020**, *11*, 4326−4330.
(47) Ma, Z.; Shi, Z.; Yang, D.; Li, Y.; Zhang, F.; Wang, L.; Chen, X.; Wu, D.; Tian, Y.; Zhang, Y.; Zhang, L.; Li, X.; Shan, C. High Color-Rendering Index and Stable White Light-Emitting Diodes by Assembling Two Broadband Emissive Self-Trapped Excitons. *Adv. Mater.* **2021**, *33*, 2001367.
(48) Ma, Z.; Shi, Z.; Qin, C.; Cui, M.; Yang, D.; Wang, X.; Wang, L.; Ji, X.; Chen, X.; Sun, J.; Wu, D.; Zhang, Y.; Li, X. J.; Zhang, L.; Shan, C. Stable Yellow Light-Emitting Devices Based on Ternary Copper Halides with Broadband Emissive Self-Trapped Excitons. *ACS Nano* **2020**, *14*, 4475−4486.
(49) Sebastia-Luna, P.; Navarro-Alapont, J.; Sessolo, M.; Palazon, F.; Bolink, H. J. Solvent-Free Synthesis and Thin-Film Deposition of Cesium Copper Halides with Bright Blue Photoluminescence. *Chem. Mater.* **2019**, *31*, 10205−10210.

https://doi.org/10.1021/acsaelm.1c01060
ACS Appl. Electron. Mater. 2022, 4, 663−671

(50) Ma, Z.; Wang, L.; Ji, X.; Chen, X.; Shi, Z. Lead-Free Metal Halide Perovskites and Perovskite Derivatives as an Environmentally Friendly Emitter for Light-Emitting Device Applications. *The Journal of Physical Chemistry Letters* **2020**, *11*, 5517−5530.
(51) Jung, Y.-K.; Han, I. T.; Kim, Y. C.; Walsh, A. Prediction of high thermoelectric performance in the low-dimensional metal halide $Cs_3Cu_2I_5$. *npj Comput. Mater.* **2021**, *7*, 51.
(52) Vashishtha, P.; Nutan, G. V. E.; Griffith, B. E.; Fang, Y.; Giovanni, D.; Jagadeeswararao, M.; Sum, T. C.; Mathews, N.; Mhaisalkar, S. G.; Hanna, J. V.; White, T. Cesium Copper Iodide Tailored Nanoplates and Nanorods for Blue, Yellow, and White Emission. *Chem. Mater.* **2019**, *31*, 9003−9011.
(53) Yao, X.; Qi, J.; Xu, W.; Jiang, X.; Gong, X.; Cao, Y. Cesium-Doped Vanadium Oxide as the Hole Extraction Layer for Efficient Perovskite Solar Cells. *ACS Omega* **2018**, *3*, 1117−1125.
(54) Liu, Y.; Yin, J.; Wang, P.; Hu, Q.; Wang, Y.; Xie, Y.; Zhao, Z.; Dong, Z.; Zhu, J.-L.; Chu, W.; Yang, N.; Wei, J.; Ma, W.; Sun, J.-L. High-Performance, Ultra-Broadband, Ultraviolet to Terahertz Photodetectors Based on Suspended Carbon Nanotube Films. *ACS Appl. Mater. Interfaces* **2018**, *10*, 36304−36311.
(55) Xu, X.; Gabor, N. M.; Alden, J. S.; van der Zande, A. M.; McEuen, P. L. Photo-Thermoelectric Effect at a Graphene Interface Junction. *Nano Lett.* **2010**, *10*, 562−566.
(56) Ouyang, B.; Zhang, K.; Yang, Y. Photocurrent Polarity Controlled by Light Wavelength in Self-Powered ZnO Nanowires/SnS Photodetector System. *iScience* **2018**, *1*, 16−23.
(57) Ma, N.; Zhang, K.; Yang, Y. Photovoltaic−Pyroelectric Coupled Effect Induced Electricity for Self-Powered Photodetector System. *Adv. Mater.* **2017**, *29*, 1703694.
(58) Zhang, K.; Wang, Z. L.; Yang, Y. Enhanced P3HT/ZnO Nanowire Array Solar Cells by Pyro-phototronic Effect. *ACS Nano* **2016**, *10*, 10331−10338.
(59) Xie, C.; Mak, C.; Tao, X.; Yan, F. Photodetectors Based on Two-Dimensional Layered Materials Beyond Graphene. *Adv. Funct. Mater.* **2017**, *27*, 1603886.
(60) Gu, Y.; Yao, X.; Geng, H.; Guan, G.; Hu, M.; Han, M. Highly Transparent, Dual-Color Emission, Heterophase $Cs_3Cu_2I_5/CsCu_2I_3$ Nanolayer for Transparent Luminescent Solar Concentrators. *ACS Appl. Mater. Interfaces* **2021**, *13*, 40798−40805.

https://doi.org/10.1021/acsaelm.1c01060
ACS Appl. Electron. Mater. 2022, 4, 663−671